Advanced Composites and Hybrid Materials (2024) 7:131
https://doi.org/10.1007/s42114-024-00932-4

RESEARCH

Combination of 3D Printing, Plasma Polymerization, and Bioactive Coatings Towards Fabrication of Eggshell Biowaste/Polycaprolactone Composite Scaffolds for Bone Regeneration

Arman Jafari[1,2,3] · Aram-Sevag Afarian[1,2,3] · Armin Amirsadeghi[4] · Patrick Piet van Vliet[2] · Mahdi Darvish[5] · Sean Watson[6] · Ali Mousavi[1,2,3] · Vahid Niknezhad[7] · Gregor Andelfinger[2,8] · Stephan Reuter[3,6,9] · Michael R. Wertheimer[6,9] · Abdellah Ajji[5,9,10] · Houman Savoji[1,2,3,10]

Received: 17 October 2023 / Revised: 19 March 2024 / Accepted: 1 July 2024 / Published online: 2 August 2024

Abstract

3D printing is a robust technique that can fabricate customized tissue-engineered scaffolds for bone regeneration. Eggshell (ES) contains bone-like compounds, which makes this biowaste an interesting material for bone tissue engineering. Here, we fabricated 3D printed scaffolds using polycaprolactone (PCL) and ES powder and investigated the effect of ES concentration on the printability, mechanical properties, and morphology of the scaffolds. It was found that ES significantly alters the surface topography of the 3D printed PCL/ES structures from smooth at 10 wt.% to irregularly shaped at 30 wt.%. Moreover, although ES agglomeration was observed at higher concentrations, no significant adverse effect on mechanical properties was observed. To enhance the scaffolds' bioactivity, we used plasma polymerization to deposit an oxygen-rich thin film coating to activate the scaffolds' surfaces. Subsequently, gentamicin (Gent), as a model bioactive agent, was grafted on the surface of the scaffolds. The Gent grafting was approved by X-ray photoelectron spectroscopy. Gent-grafted scaffolds showed over 80% and 99.9% bacteria reduction against *Pseudomonas aeruginosa* after 1 and 24 h, respectively. Biocompatibility assessments using fibroblasts showed both high cell viability (over 90%) and cell proliferation during 23 days of culture. Using mesenchymal stem/stromal cells, successful osteoblast differentiation was observed, as shown by upregulation of Runt-related transcription factor 2 (RUNX2) and osteocalcin genes along with increased mineralization. Overall, our findings demonstrated the great potential of the 3D printed scaffolds with improved bioactivity for bone tissue engineering.

Keywords Eggshell · Green chemistry · 3D printing · Plasma polymerization · Tissue engineering · Bone regeneration

✉ Houman Savoji
houman.savoji@umontreal.ca

[1] Institute of Biomedical Engineering, Department of Pharmacology and Physiology, Faculty of Medicine, University of Montreal, Montreal, QC H3T 1J4, Canada

[2] Research Center, Centre Hospitalier Universitaire Sainte-Justine, Montreal, QC H3T 1C5, Canada

[3] Montreal TransMedTech Institute, Montreal, QC H3T 1J4, Canada

[4] Transplant Research Center, Shiraz University of Medical Science, Shiraz 71345-1978, Iran

[5] Department of Chemical Engineering, Polytechnique Montréal, Montréal, Québec H3C 3A7, Canada

[6] Department of Engineering Physics, Polytechnique Montréal, Montréal, Québec H3C 3A7, Canada

[7] Program in Craniofacial Biology, Department of Cell and Tissue Biology, University of California, San Francisco, CA, USA

[8] Département de Pédiatrie, Université de Montréal, Montréal, QC, Canada

[9] Institute of Biomedical Engineering, Polytechnique Montréal, Montréal, Québec H3C 3A7, Canada

[10] Center for Applied Research On Polymers and Composites (CREPEC), Montreal, QC, Canada

1 Introduction

Tissue engineering is one of the fastest-growing fields that aims to repair or replace damaged tissues. The presence of a scaffold, which acts as a temporary environment for cell growth and tissue development, is crucial in tissue engineering [1, 2]. Such scaffold would attract endogenous cells to populate, infiltrate, remodel, and form a mature tissue from this "blueprint". The implementation of cells and/or bioactive molecules could improve the efficiency of the implanted scaffolds [3–5]. Depending on the targeted tissue, different strategies, such as electrospinning, molding, gas foaming, freeze-drawing, and 3D printing could be employed to produce tissue-engineered scaffolds [6–9]. Among these strategies, three-dimensional (3D) printing has shown to be a versatile technique for producing scaffolds with high efficiency, controllability, and precision [10, 11]. In 3D printing, a computer-aided design (CAD) of a 3D object is used. For printing, the design is divided into several two-dimensional (2D) structures (layers), and through a layer-by-layer assembly, the 3D object is formed [12].

Bone is a unique tissue that provides the body with the required structural support and protection for internal soft tissues. Bone also serves as a mineral reservoir and coordinates blood production [13, 14]. Bone tissue damage and disorder can occur for several reasons, ranging from accidents to diseases and traumas [15, 16]. The implantation of artificial bone grafts has been considered a standard to facilitate bone regeneration. Bone regeneration is a complex cascade that needs the orchestrated function of several cell types, including immune cells, osteoblasts, and stem cells [17]. Conventionally, allografts and autografts are considered the best options for implantation. However, tissue-engineered bone scaffolds are emerging as appealing alternatives. Engineered scaffolds can evade several drawbacks of former traditional approaches (i.e., allografts and autografts), including donor shortage, immune responses, and chance of body rejection [18–20]. Based on the selected materials, tissue-engineered bone scaffolds can improve healing by enhanced vascularization, remodeling, biodegradation, and complete integration with the host body [21]. Considering its extracellular (ECM) composition, bone is a biocomposite formed from mineralized and organic compounds [22]. Polymers could be a suitable choice for mimicking the organic phase of bone due to their biocompatibility, biodegradation, and ease of process [23]. Among others, polycaprolactone (PCL) is a Food and Drug Administration (FDA) approved synthetic polyester that is widely used for the fabrication of tissue-engineered scaffolds [24, 25]. Along the aforementioned characteristics, PCL has a low degradation rate, providing bone tissue enough time for remodeling [26]. In addition, PCL has a relatively low melting point that facilitates its printing using melt-extrusion-based approaches [27].

In recent years, due to global concerns for energy consumption and pollution, recycling waste products and making high-value products have opened new perspectives on a greener and more sustainable planet. As tissue engineering is an emerging and rapidly growing industry, using biowastes in scaffolds can help reduce the final price and make the process more sustainable and greener. For instance, tons of eggshells (ES) (8.58 million metric tons according to the Food and Agriculture Organization (FAO)) are discarded yearly as biowastes through industries and household consumption [28]. Nevertheless, this naturally occurring biomaterial has been shown to have many applications ranging from catalyst production to agriculture and biomedical engineering [29]. Like natural human bone, ES is a calcium-based material that contains other components, including magnesium, sodium, and potassium [30]. In addition, the abundance of ES makes it a highly desirable material for bone tissue engineering. Huang et al. developed a composite scaffold for bone tissue engineering using ES particles grafted with magnesium oxide nanoparticles, carboxymethyl chitosan, and bone morphogenetic protein 2 [31]. It was shown that the fabricated scaffold has suitable biomineralization and osteogenic differentiation properties. In another work, Wu et al. fabricated Gelatin methacryoyl (GelMA)/ES particles composite scaffolds for bone regeneration, showing this structure's potency to facilitate the differentiation and biomineralization of pre-osteoblast cells. The obtained results also revealed that the osteogenic improvements directly relate to the presence of the ES particles in the scaffolds. Moreover, subcutaneous implantation demonstrated that ES composite scaffold has biocompatibility without any sign of inflammatory response [32].

One of the most challenging issues in developing and implanting an artificial scaffold in the human body is the possibility of infection and subsequent severe inflammation due to bacterial growth at the implantation site. The occurrence of such complications will then lead to implant rejection and the necessity of a follow-up surgery [33]. This would be even more prominent in invasive surgical procedures such as bone implantations with an infection risk of 10 to 50% [34, 35]. As a result, having proper and efficient antibacterial properties is of great importance for bone tissue-engineered scaffolds. Several drug delivery approaches have been successfully investigated to fabricate bioactive platforms to tackle this issue. For example, Paris et al. fabricated a porous composite scaffold containing agarose, hydroxycarbonate apatite, and mesoporous silica. It was shown that both the loaded scaffolds and the mesoporous silica nanoparticles with an antibiotic drug had rapid and prolonged antibacterial effects. Besides, this

scaffold could provide an adequate antibiotic effect at the initial state to kill bacteria as well as a sustained release over a longer period, which was shown to be effective against *Staphylococcus aureus* [36].

Surface modification of scaffolds has shown to be promising as it opens many possibilities for further modification of 'scaffolds' properties. Among others, plasma treatment has several advantages over more traditional wet chemical modification, such as high efficiency, less toxicity, and the production of less chemical waste, leading to a greener and more sustainable procedure [37, 38]. One of the most powerful techniques developed by our team [39–42] is the deposition of a plasma-polymerized coating to introduce functional groups on the scaffolds to promote bioactive properties (e.g., cell adhesion) or enable biomolecule immobilization [43, 44]. Plasma-polymerized thin film coatings have been shown to induce high-density and stable functional groups that are more effective than conventional plasma treatment/modification techniques. For example, Savoji et al. coated poly(ethylene terephthalate) (PET) nanofibers with nitrogen-rich plasma polymerized coating and compared human umbilical vein endothelial cells (HUVEC) adhesion and growth on plasma-coated and non-coated scaffolds [45]. It was observed that plasma coating has significantly improved cell adhesion and growth on the nanofibrous scaffolds. Many studies have also used oxygen-rich plasma coatings to improve polymers' hydrophilicity and surface functionality [39–42, 46]. The oxygen-rich plasma polymerized coatings can be applied to functionalize the scaffolds' surfaces by depositing a thin film containing carboxy groups (-COOH), which can later be used for further grafting [47, 48]. Boespflug et al. reported an oxygen-rich plasma polymerized coating that also supported HUVEC adhesion and growth [49].

In the current study, we developed a bioactive antibacterial 3D printed scaffold using PCL and different concentrations of ES biowaste powder to show the potential of this composite for bone tissue engineering. A highly efficient plasma polymerization technique was employed on the scaffolds to further activate their surface and enable the grafting of an antibacterial biomolecule (i.e., gentamicin sulfate (Gent)). Gent was grafted on plasma-polymerized coated scaffolds. Different characterization techniques were used to evaluate the physicochemical properties of the composite scaffolds containing various ES concentrations. Moreover, the effect of plasma polymerization on Gent grafting was investigated. Finally, the scaffolds' biocompatibility was evaluated using somatic fibroblast cells and mesenchymal stem/stromal cells. The obtained results showed the success of 3D printing and surface bioactivation, along with the potency of the differentiation of the cells cultured on the scaffolds toward osteoblasts, confirming the possibility of using these scaffolds for bone tissue engineering applications.

2 Materials and Methods

2.1 Materials

PCL (Mn = 80,000), chloroform, 1-Ethyl-3-(3-dimethyl aminopropyl) carbodiimide (EDC), N-Hydroxysuccinimide (NHS), and gentamicin sulfate (Gent) were purchased from Sigma-Aldrich, USA. Ostrich eggs were bought from a local ostrich farm in Quebec, Canada. Human bone marrow-derived mesenchymal stem/stromal cells (hBMSCs), and RoosterNourish™-MSC media were obtained from RoosterBio, USA. Dulbecco's Modified Eagle Medium-F12 (DMEM-F12), fetal bovine serum (FBS), Penicillin–Streptomycin (pen/strep), and StemPro™ Osteogenesis Differentiation Kit (ODM) were all acquired from Gibco (ThermoFisher Scientific, USA). LIVE/DEAD™ Viability/Cytotoxicity Kit was obtained from Invitrogen, USA.

2.2 Composite Preparation

Fresh ostrich eggs were cracked to remove the egg white and yolk. The shells were then washed thoroughly with excess distilled water, the eggshell membrane was peeled off, and the ESs were rewashed with excess distilled water. Following drying, ESs were ground using a ball mill (8000 M, Spex). The morphology of the ES powder was investigated using field emission scanning electron microscopy (FE-SEM, JSM-7600 TFE, JEOL, Japan).

To prepare the PCL/ES composites, PCL with 10, 20, and 30 wt.% of ES powder were dissolved in chloroform using a magnetic stirrer. Subsequently, the solutions were sonicated using an ultrasound machine for 1 h to disperse the particles. Solutions were then poured into glass Petri dishes and put under a vacuum for two days to ensure complete solvent removal.

2.3 3D Printing and Printability Assessment

Composite sheets of PCL/ES were loaded into a thermoplastic printhead of BIO X6 bioprinter (CELLINK, USA) to print the scaffolds. The effect of temperature was investigated on the printing fidelity by printing the scaffolds at various temperatures and measuring the quality of the 3D printed constructs using a stereo microscope (M205, Leica Microsystems, Canada). The mean fiber diameter ± standard deviation (SD) was calculated by analyzing 20 different fibers with ImageJ software (National Institutes of Health). Based on these preliminary examinations, appropriate printing parameters were chosen to be: printing pressure: 600 kPa, printing speed: 2 mm/s, printing temperature:

180 °C. Finally, printed scaffolds were collected and kept in a dry place for further experiments.

2.4 Fourier Transform Infrared Spectroscopy (FTIR)

FTIR was used to investigate the chemical composition of the scaffolds. The attenuated total reflectance-Fourier transform infrared (ATR-FTIR) apparatus (Spectrum 65, Perkin Elmer, USA) recorded transmittance of the samples in the range of 600 – 4,000 cm^{-1} with 2 cm^{-1} resolution and a total number of 32 scans.

2.5 Thermogravimetric Analysis (TGA)

To investigate the thermal stability of composites for printing, TGA was performed using a Q500 (TA instruments, USA) under a dry nitrogen atmosphere from room temperature to 800 °C, with a heating rate of 10 °C/min.

2.6 Differential Scanning Calorimetry (DSC)

DSC curves were obtained through a cycle of heating, cooling, and heating the samples from − 90 to 200 °C, with a 10 °C/min temperature change rate. For this purpose, around 5 mg of samples were weighed, filled into hermetic pans, and loaded into the Q2000 (TA instruments, USA) machine. Tests were performed under nitrogen gas.

2.7 X-ray Diffractometry (XRD)

XRD analysis was conducted to confirm the presence of ES particles within the 3D printed constructs. Samples were prepared based on manufacturer protocols to be tested by the D8 advance apparatus (Bruker, Germany).

2.8 Scanning *Electron* Microscopy (SEM)

SEM imaging was implemented to investigate 'scaffolds' surface morphology, fiber–fiber interaction, 'fiber's internal morphology, and ES distribution using a benchtop SEM machine (TM3030Plus, Hitachi, Japan). Before imaging, samples were coated with chromium using a Q150R-ES (Quorum Technologies, England) sputter coater. In addition, further ES distribution in printed filaments was investigated through elemental mapping analyzed by a dispersive X-ray (EDX) approach.

2.9 Mechanical Characterization

The effect of different ES contents on the mechanical behavior of the 3D printed scaffolds has been investigated by MTS Insight Electromechanical Testing Machine (MTS Systems Corporation, USA). Unconfined compression tests were performed on the samples ($n = 6$) by compressing 3D printed cylindrical scaffolds (1 cm diameter, 5 mm height, and 25% infill density) at a rate of 0.5 mm/min [50]. Obtained stress–strain data was then used to calculate compression modulus in the linear region.

2.10 Plasma Polymerization

Plasma polymerization on PCL/ES10 3D printed scaffolds was carried out in a capacitively-coupled (13.56 MHz, ENI) radio-frequency (r.f.) glow discharge plasma reactor (Fig. 1). The plasma was created in a cylindrical aluminum/steel vacuum chamber, approximately 20 cm in diameter and 20 cm high; this system was already illustrated earlier, so we will refer the reader to these works [40]. A turbo-molecular pump, backed by a two-stage rotary vane pump, was used to evacuate the chamber to a base pressure of $< 10^{-4}$ Pa. Flows of high-purity feed gas were then admitted into the chamber using electronic flow meter/controllers (Vacuum General Inc.) and a ""shower head"" gas distributor (10 cm in diameter). Plasma was generated under mild conditions, with applied r.f. power $p = 10$ W (resulting in a negative d.c. bias voltage, $V_B = -40$ V), and at an operating pressure $p = 80$ Pa, maintained constant by a butterfly throttle valve, in combination with a capacitive pressure gauge (Baratron, MKS Instruments). Reagent gas mixture was used as follows: ethylene (C_2H_4) was combined with molecular oxygen diluted in argon (10% O_2 + 90% Ar) to obtain low-pressure plasma-polymerized (L-PP) thin coatings containing oxygen. The flow rate of C_2H_4 (F_{C2H4}) was kept constant at 20 standard cubic centimeters per minute (sccm), while the other reagent gas flow could be varied; the gas flow ratio R (F_{O2}/ F_{C2H4}) in this case was 0.15. Note that O_2 was diluted in argon to minimize the occurrence of competing ablation (etching) by atomic oxygen. Based on our earlier work, the

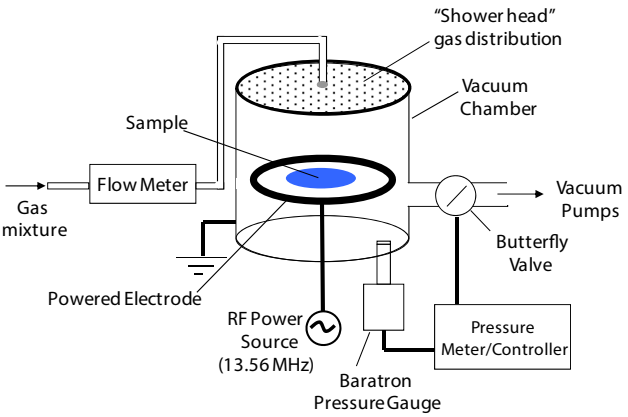

Fig. 1 Schematic views of the low-pressure capacitively-coupled r.f. reactor, used for depositing oxygen-rich thin organic thin. Reproduced with permission from Ref[23]

above-cited R-value resulted in coatings with maximum hetero-atom content and low solubility in water or cell culture medium. The plasma-assisted polymerization was continued for 10 min, resulting in a roughly 100 nm thick coating [39, 41, 42]. After the reaction was terminated, surface-coated 3D printed scaffolds were retrieved and used immediately for further experiments.

2.11 Gentamicin Grafting

After plasma polymerization, Gent, as a model bioactive agent, was grafted on the surface of the 3D printed plasma-polymerized constructs using EDC/NHS chemistry (hereafter referred to as Gent-grafted PCL/ES10) [51]. The surface bioactivation and Gent grafting were done in two steps. First, plasma-polymerized constructs were soaked in an aqueous solution of EDC (3 mM) and NHS (7.5 mM) for 15 min. Subsequently, they were washed with distilled water and merged into a 40 mg/mL solution of Gent (in phosphate buffer saline (PBS)) for 2 h at room temperature. Afterward, samples were rewashed with distilled water, dried, and stored in a dry environment for further use.

2.12 X-Ray Photoelectron Spectroscopy (XPS)

Surface characterization of plasma-polymerized and plasma-polymerized Gent grafted scaffolds was evaluated by VG Escalab 250Xi (ThermoFisher Scientific, USA) using monochromatic Al Kα as the radiation source. A 900 µm diameter in a depth of < 10 nm was scanned for the analysis. Spectra were recorded at zero-degree takeoff angle. Data analysis and quantification were completed using Avantage v4.12 software (Thermo Electron Corporation) through peak area integration, after Shirley-type background subtraction, and using sensitivity factors from the Wagner table.

2.13 Contact Angle Measurement

The change in surface hydrophilicity was evaluated using water contact angle (WCA) measurement using a sessile drop method (Dataphysics OCA20). Water droplets of 4 µL were placed on the surface of the 3D printed scaffolds, and the static contact angles were measured using obtained images.

2.14 Antibacterial Activity

The antibacterial activity of Gent-grafted composites was tested against the gram-negative bacteria *Pseudomonas aeruginosa (P. aeruginosa)* based on standard ASTM E2149-20 with slight modifications. Briefly, bacteria were inoculated overnight in LB agar (Liquid inoculum). 50 mg of scaffolds were weighed and incubated in 5 ml of bacterial solution (~ 1×10^6 CFU/mL) in PBS. Samples were then put in a shaker incubator set at 37 °C with a shaking rate of 170 rpm. At specified intervals, a certain amount of bacterial suspension was retrieved, diluted, and used for standard plate counting. Bacterial suspensions without the scaffolds were used as control.

2.15 Biocompatibility and Cell Proliferation Assessment

The cytotoxicity of Gent-grafted 3D printed scaffolds was investigated through the culture of 3T3 mouse fibroblast cells on the scaffolds. In brief, 3T3 cells were passaged using a complete medium (DMEM-F12 containing 10% FBS and 1% pen/strep) until reaching ~ 80% confluency. Subsequently, cells were detached from the 'flask's surface using trypsin–EDTA and counted. Scaffolds were ultraviolet (UV) sterilized for 30 min on each side. 1×10^5 cells were cultured on the scaffolds and incubated for 2 h in 12 well plates. Afterwards, scaffolds were transferred into new plates and cultured with the complete medium for 23 days in an incubator set at 37 °C with 5% CO_2.

At specific time points, samples were removed from the incubator and stained with live/dead stains per the 'manufacturer's protocol. This was achieved by incubating scaffolds in 1 mL of live/dead solution for 30 min. The scaffolds were then rinsed with Dulbecco's phosphate-buffered saline (DPBS) and were used for imaging using a confocal microscope (TCS SP8-DLS, Leica Microsystems).

2.16 Stem/Stromal Cell Culture and Differentiation

hBMSCs were passaged on cell culture flasks using specific complete media (RoosterNourish, Rooster Bio, USA), similar to the previous section. After counting, 2×10^5 hBMSCs were incubated on the scaffolds in the complete media for 4 days. To induce cell differentiation, scaffolds were incubated for 21 days in the ODM. The ODM was changed every 3 days. At the end of the differentiation period, the samples were used for alizarin red S staining, reverse transcription-polymerase chain reaction (RT-PCR) analysis, and fluorescent imaging.

2.16.1 Alizarin Red Staining

After the culture of hBMSCs in ODM for 21 days, the extent of mineralization was evaluated using alizarin red S staining. Following the culture, cells were washed with DPBS and fixed using a 4% paraformaldehyde solution for 30 min. Subsequently, cells were washed twice with distilled water and stained with 2% alizarin red S solution for around 2 min. After staining, the samples were rinsed and imaged with a stereo microscope (Leica M205).

2.16.2 RNA Isolation and Quantitative Reverse Transcription-Polymerase Chain Reaction (RT-qPCR)

RNA was isolated with the ReliaPrep RNA Miniprep kit (Promega Z6111) per the manufacturer's protocol and quantified on a Thermo Scientific NanoDrop spectrophotometer. 500 ng RNA was used to generate cDNA with Superscript IV reverse transcriptase (Thermo Scientific 18,090,010) and random hexamers (Thermo Scientific N8080127). Quantitative PCR was performed as technical triplicates with SYBR Green (Roche Fast Start, Millipore Sigma 4,913,850,001) on a BioRad CFX real-time PCR system. Data were analyzed with BioRad CFX Maestro. PCR products were checked for specificity via melt-curve and gel electrophoresis analyses. PCR primers were designed with the NCBI Primer-BLAST tool. Primer specifics can be found in Supplementary Table 1. Baseline thresholds were set in the exponential phase for each gene, and the resulting Ct values were used to calculate the $2^{-\Delta Ct}$ for each gene versus the reference glyceraldehyde-3-phosphate dehydrogenase (GAPDH).

2.16.3 Fluorescent Staining

The cytoskeletal structure of cells at the end of the differentiation process was investigated using Phallodin-iFlour 594 (Abcam, USA) and 4',6-diamidino-2-phenylindole dihydrochloride (DAPI, Invitrogen) staining. After removing the scaffolds from the media, they were washed with DPBS and fixed with 4% paraformaldehyde. Later, 0.1% Triton X-100 was used to permeabilize the cells, and phalloidin solution was introduced and incubated for 70 min. DAPI staining was also done similarly based on the 'manufacturer's protocol. Finally, the scaffolds were rinsed and imaged using a TCS SP8-DLS confocal microscope.

2.17 Statistical Analysis

Analysis of variance (ANOVA) tests were applied to the obtained data to determine statistical significance. All the analyses were performed in triplicate experiments (unless otherwise indicated) and mean ± SD was reported. *P* values under 0.05 have been considered statistically significant ($*p<0.05$, $**p<0.01$, $***p<0.001$, and $****p<0.0001$).

3 Results and Discussion

3.1 Composite Scaffold Characterization

Figure 2a shows the FTIR spectra of pure PCL, ES, and PCL/ES composite scaffolds at different ES concentrations. The typical characteristic peaks of PCL at 1166 (symmetric C – O – C stretching) and 1725 (C = O stretching) cm^{-1} were observed [52, 53]. ES, mainly composed of calcium carbonate ($CaCO_3$), showed 3 characteristic peaks at 713, 874, and 1409 cm^{-1} corresponding to C – O

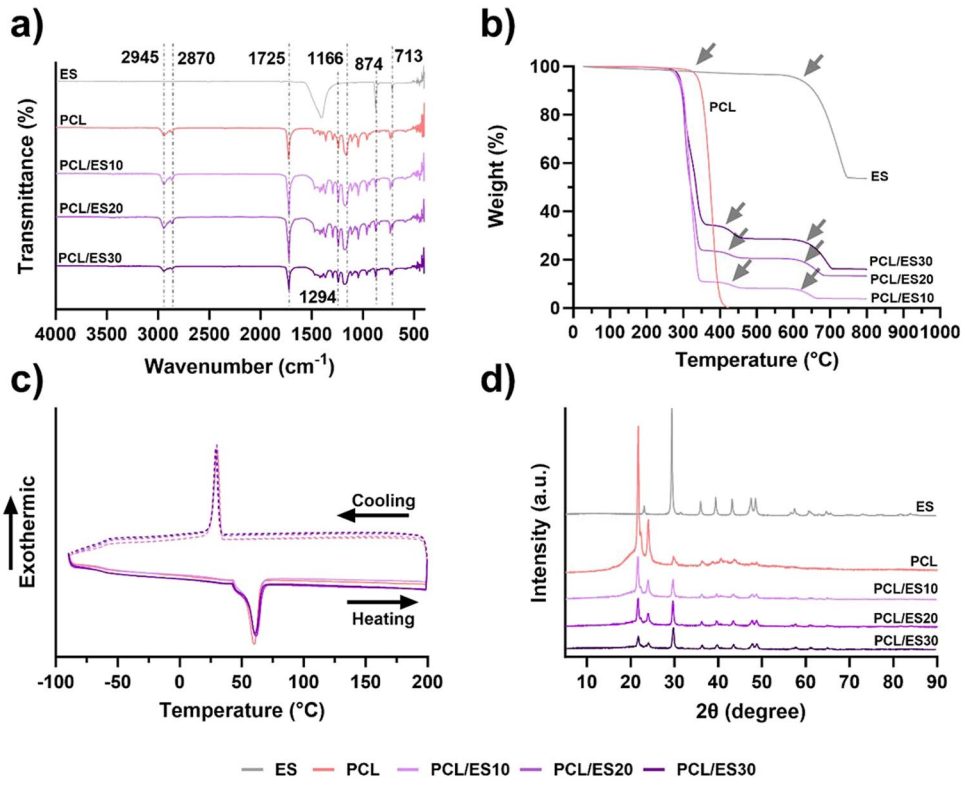

Fig. 2 Physicochemical characterization of composite PCL/ES scaffolds: (**a**) FTIR spectra, (**b**) TGA analysis, (**c**) DSC, and (**d**) XRD spectra of PCL, ES, and PCL/ES composite scaffolds with different concentrations of ES. Arrows in panel b show the start point of the decomposition stages

bands [32, 54]. As expected, PCL/ES composite scaffolds showed all the characteristic peaks of both PCL and ES, with a slight shift C—O—C stretching from 1166 to 1177 cm^{-1} due to PCL chains interaction with ES [52].

The thermal properties of composite scaffolds and pure compounds were also investigated using TGA analysis (Fig. 2b). The thermal stability of the materials and composites was of specific importance in this work since the 3D printing process was conducted at elevated temperatures. Consequently, it was critically important to ensure the materials did not show any signs of degradation at the selected printing temperature. The results showed that ES was thermally stable up to temperatures around 600 °C. Above this temperature, ES started to decompose, losing a total weight of 43% up to 726 °C. Further temperature increases up to 800 °C did not affect the ES, and no additional weight loss was observed. The ES weight loss from 600 to 726 °C was due to the decomposition of $CaCO_3$ into calcium oxide (CaO) and CO_2, in which CaO remained as a solid, and CO_2 was released in the air as a gas [54]. Recorded data for PCL also showed that the polymer was stable to around 300 °C, then went through a sharp decrease in weight, and finally fully decomposed at 378 °C. PCL/ES10, PCL/ES20, and PCL/ES30 showed a sharp decrease in weight (88.86, 75.92, and 65.40%, respectively) starting from around 250 °C, that was followed by a second less steep decrease in weight (2.63, 3.14, and 5.65%, respectively) at 434 °C. These weight-loss regions could be related to PCL decomposition as the combined weight loss of the first and second regions was equivalent to the PCL content of the scaffolds. The reason for the formation of the two regions was most probably due to the presence of ES. Besides, the PCL/ES composite scaffolds showed lower onset decomposition temperatures than pristine PCL. Previous studies have shown that the nature of $CaCO_3$, the main component of ES, could act as a catalyst to depolymerize the ester bonds of polyesters [55, 56]. The subsequent weight loss was observed at 600 °C due to the decomposition of ES. Overall, all the composite scaffolds were shown to be thermally stable at the printing temperature, showing that no thermal degradation occurs during printing.

The DSC analysis of PCL and composite scaffolds showed an endothermic melting point at 56.88 °C during the second heating cycle and an exothermic crystallization peak during the cooling cycle at 28.55 °C. The obtained results showed that the addition of ES did not change PCL's melting point or crystallization temperature. Moreover, the degree of crystallinity was calculated to be 45.3% which is in agreement with previous reports [57]. Incorporation of ES resulted in no significant change in the crystallinity as for PCL/ES10, PCL/ES20, and PCL/ES30 the crystallinity was calculated to be 46.2, 48.9, and 44.9, respectively.

Further investigation on the presence and incorporation of ES into PCL was conducted using XRD (Fig. 2d). XRD analysis of ES powder showed a sharp peak at $2\theta = 29.45°$and several other smaller peaks at $2\theta = 36.1°$, 39.54°, 43.59°, 48.65°, and 48.66°), proving that ES was mainly composed of $CaCO_3$ [58]. PCL is a biodegradable polyester that is known to have a semi-crystalline structure. The XRD diffraction pattern of PCL also showed the two characteristic crystalline peaks at $2\theta = 21.73°$ and 24.09° relating to the (110) and (200) planes of the orthorhombic crystal structures, respectively [59]. PCL/ES composite scaffolds showed both characteristic peaks of PCL and ES; however, the intensity of PCL crystalline peaks decreased as the concentration of the PCL decreased.

3.2 3D Printing

To find the suitable conditions for 3D printing of PCL/ES scaffolds and the printing window, a series of preliminary printing studies on PCL and PCL/ES were performed. Figure 3 summarizes the results related to the adjustment of printing temperature. A printing temperature range of 140 to 190 °C was investigated, far below the set point of decomposition obtained by TGA analysis. It was observed that increasing the printing temperature from 140 to 180 °C improved the quality of printing (Fig. 3). More increase in printing temperature to 190 °C resulted in a significant deviation between the printed filament and nozzle diameter and reduced printing fidelity. The fiber diameter was shown to be larger by increasing the temperature due to the PC Lmelt's viscous behavior at higher temperatures [60]. Higher temperature leads to lower viscosity; thus, the molten polymer's flow rate increases, which means more materials are extruded at a constant printing pressure [61]. Furthermore, the effect of printing temperature on the printability of PCL/ES20 has also been investigated. The results showed that the PCL/ES20 composite scaffolds had lower fiber diameters at particular temperatures compared to pure PCL scaffolds. This was due to the addition of ES particles, which increased the viscosity and elastic behavior of the polymer melt, as had already been shown by previous studies [62, 63]. This phenomenon makes the flow of the polymer melt more difficult. As a result, less material could be extruded from the nozzle, and fiber diameter was decreased. It could be seen that the addition of 20% ES improves the quality of the printed structure. Overall, the results showed that 180 °C was also suitable for printing PCL/ES composite scaffolds; thus, 180 °C was chosen as an optimum printing temperature for further printing.

3.3 SEM and EDX Elemental Mapping

SEM images and EDX elemental mapping were performed to study the morphology of the printed scaffolds. For bare

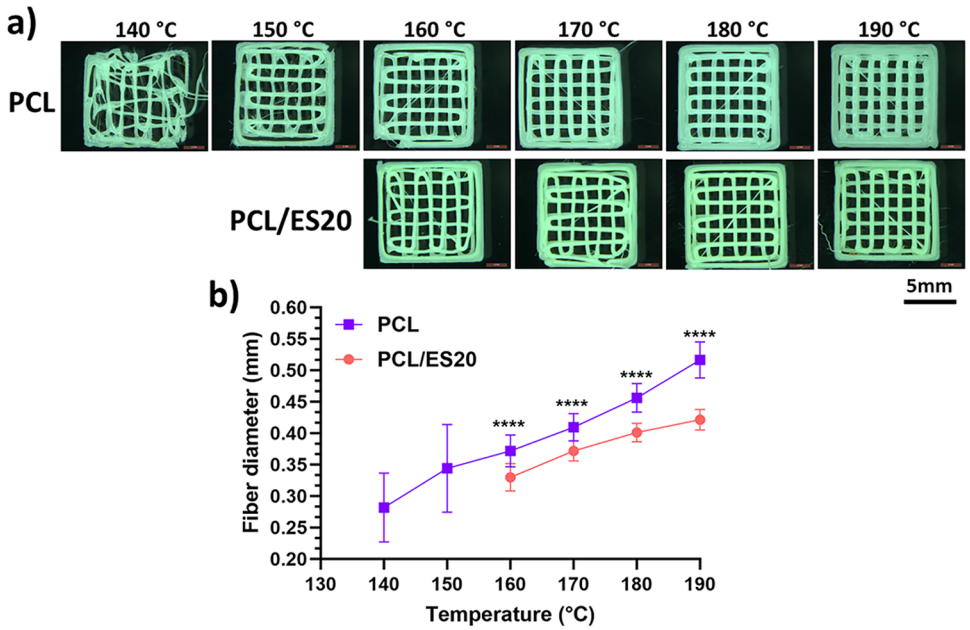

Fig. 3 Evaluating the printability of the composites. (**a**) Optical images obtained from 3D printed PCL and PCL/ES20 scaffolds at different temperatures and (**b**) calculated fiber diameters as a function of temperature for PCL and PCL/ES20. (****$p < 0.0001$)

PCL, the images obtained revealed a smooth surface for the filaments and adhesion between layers (Fig. 4 and Figure S1 Supporting Information). The SEM images also showed that the surface morphology of PCL/ES composite scaffolds remained relatively smooth, up to 20% ES. Nonetheless, the incorporation of 30% ES into the composite significantly altered the surface morphology. 3D printed PCL/ES30 scaffolds showed higher surface roughness with a rough, irregularly shaped filament surface. On the other hand, inter-layer adhesion of filaments seemed to be still present in all PCL/ES scaffolds, assuring the possibility of printing multi-layer constructs (Figure S1 Supporting Information).

Moreover, surface and cross-sectional EDX elemental mappings were recorded to further investigate ES particle dispersion within printed constructs (Figure S2 Supporting Information). Low magnification surface mappings showed the presence of ES particles all over the constructs. However, higher magnifications showed the existence of large agglomerates of ES particles in PCL/ES20 and PCL/ES30. These observations could be expected since particles tend to agglomerate to reduce their surface energy, and higher concentrations of particles facilitate this phenomenon [62, 64]. This higher incidence of particle agglomeration and its effects on flow behavior could be a reason for the observed rough and irregular surface of PCL/ES30 scaffolds.

3.4 Mechanical Analysis

The mechanical properties of the scaffolds have been studied. The obtained results showed that 3D printed pure PCL scaffolds had a compressive modulus of 19.7 ± 4.1 MPa. The addition of 10% ES slightly increased the modulus to 20.1 ± 1.16 MPa for PCL/ES10 scaffolds. On the other hand, 20 and 30% of ES reduced the modulus of PCL/ES20 and PCL/ES30 scaffolds to 16.0 ± 2.5 and 16.1 ± 5.7 MPa, respectively (Fig. 4e and Figure S3 Supporting Information). The addition of more than 20% ES was shown to affect the compressive modulus of the scaffolds adversely. However, regardless of ES concentration, none of the samples revealed any signs of macroscopic crack or break during the tests up to 90% compressive strains (Figure S3 Supporting Information). As was shown in EDX results (Figure S2 Supporting Information), an increase in ES concentration led to the formation of agglomerates. The presence of agglomerates acts as defect points, resulting in lower mechanical properties [65]. Natural human bones can be generally categorized into cortical and cancellous bones. Cortical bones are dense and hard, while cancellous bones are spongy and porous. Due to their different internal structure and functions, these types of bones possess different mechanical properties. The compressive modulus of cortical bones ranges from 100 to 200 MPa, while this is between 2 to 20 MPa for cancellous bones [66]. The compressive modulus of the fabricated composite scaffolds was in the range of cancellous bone, showing their potential application for cancellous bone regeneration. Notably, the obtained compressive modulus was influenced by the infill percentage of the printing design (25%). Previous studies have also shown that increasing the infill percentage could significantly improve compressive modulus [67, 68]. Since PCL/ES20 and PCL/ES30 scaffolds showed increased surface irregularities, agglomeration of ES within their structure, and reduced mechanical properties, PCL/ES10 was selected for subsequent tests.

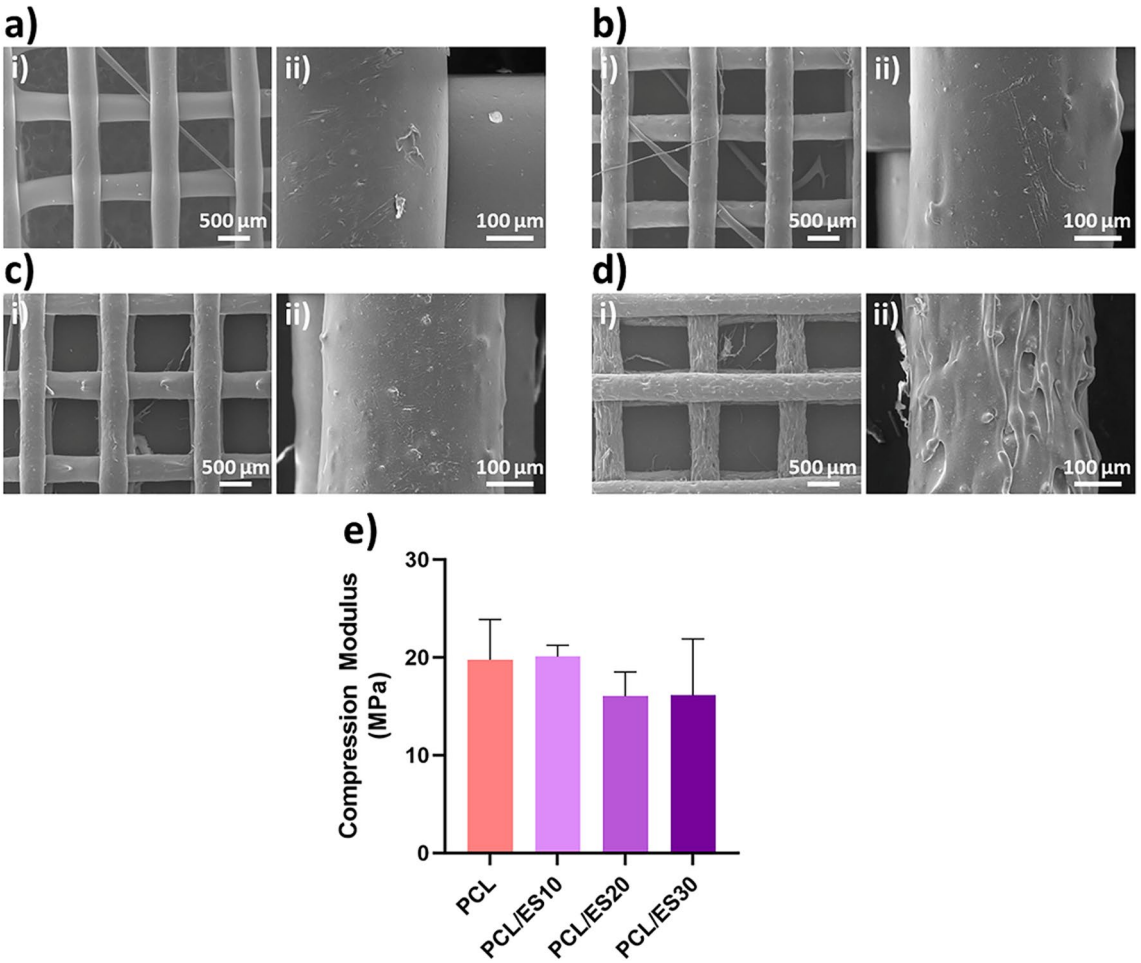

Fig. 4 Evaluation of the surface morphology and mechanical properties of the 3D printed scaffolds. SEM images showing the surface morphology of (**a**) PCL, (**b**) PCL/ES10, (**c**) PCL/ES20, and (**d**) PCL/ES30 scaffolds at i) 40×and ii) 300×magnifications. (**e**) Compressive modulus of the pristine and composite scaffolds containing different amounts of ES. Statistical analysis showed no significant difference among the groups ($P > 0.5$)

3.5 Plasma Polymerization and Gent Grafting

Plasma polymerization is a well-established green and sustainable procedure for promoting the bioactivity of scaffold and implant surfaces. It is possible to introduce various functional groups on the surface of a material that could alter the surface properties, such as hydrophilicity, or be used for further modifications (e.g., growth factor and biomolecule grafting and immobilization). Table 1 summarizes the atomic concentrations of elements recorded from the XPS of oxygen-rich plasma-polymer coated PCL/ES10 and subsequent Gent-grafted PCL/ES10 scaffold. As expected, the former (coated) PCL/ES10 scaffold showed only the presence of carbon and oxygen [69]. After Gent grafting, XPS results showed the presence of nitrogen and sulfur, which were attributed to the presence of the gentamicin sulfate on the surface of scaffolds, confirming that the grafting of Gent took place on the scaffolds.

Further detailed surface chemistry analysis was achieved through high-resolution XPS (Fig. 5). For the plasma-polymerized PCL/ES10 scaffolds, the C1s and O1s spectra were fitted with C – C (peak binding energy (BE) = 285), C – O (peak BE = 286.5), and C = O (peak BE = 532.2). In addition, the N1s spectra for this scaffold did not show any peak, reconfirming the absence of any nitrogen-related bonds. On the other

Table 1 Summary of elemental analysis of samples obtained by XPS

Sample	[C] (%at.)	[O] (%at.)	[N] (%at.)	[S] (%at.)
Plasma-polymerized PCL/ES10	71.1	28.9	0	0
Gent-grafted PCL/ES10	61.9	29.3	6.8	2.0

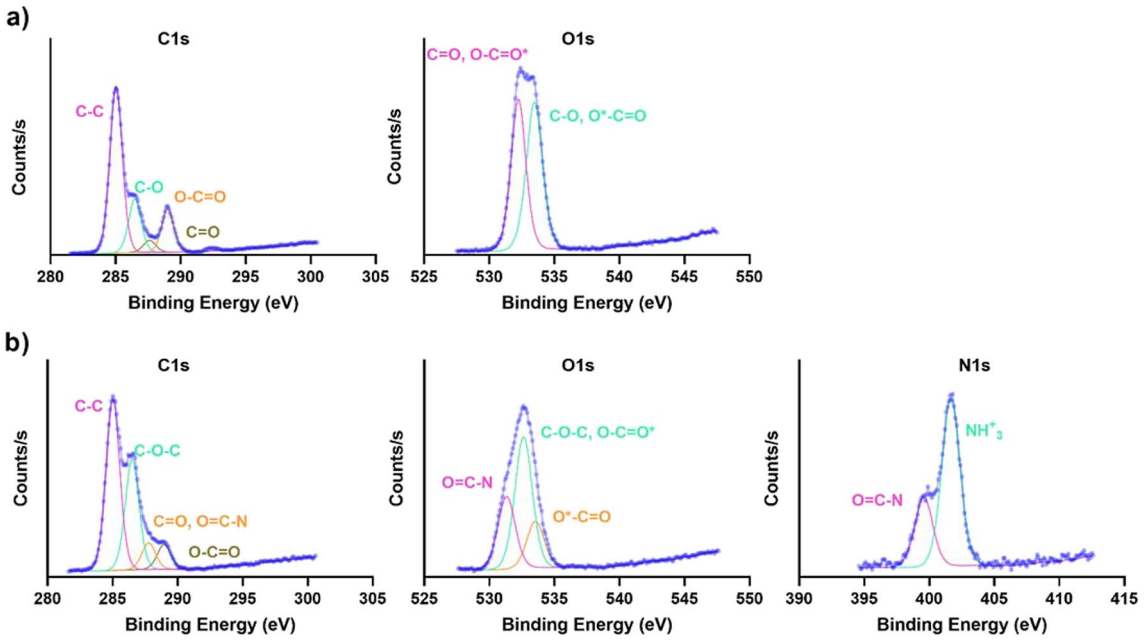

Fig. 5 Analysis of plasma polymerization on the surface of the 3D printed scaffolds. High-resolution XPS spectra (C1s, O1s, and N1s) for (**a**) plasma-polymerized PCL/ES10 and (**b**) Gent-grafted PCL/ES10

hand, the surface grafting of Gent on the plasma-polymerized PCL/ES10 scaffolds led to the presence of nitrogen-associated peaks, along with other peaks related to oxygen plasma polymerization in the high-resolution XPS spectra (Fig. 5b). More specifically, the N1s spectra showed peaks of C – N (peak BE = 399.6) and NH_3^+ (peak BE = 401.7), confirming Gent's presence and grafting on the scaffolds. The obtained results are in agreement with previous works in which Gent was grafted to the surface of scaffolds [51, 70].

The contact angle measurement of the plasma-polymerized and pristine scaffolds showed a significant increase in surface hydrophilicity. The water contact angle of non-coated PCL scaffolds was 93.1 ± 2.7 deg. (Figure S4 Supporting Information). However, after plasma-polymerization, the surface hydrophilicity significantly increased, making it impossible to measure the actual contact angle (Figure S5 Supporting Information).

3.6 Antibacterial Properties

Substantial antibacterial properties are crucial for successful implantation after surgery due to the high risk of bacterial infection [34]. Recent studies showed that *P. aeruginosa* is responsible for almost 14% of total infections related to open fractures [71]. Moreover, infection with *P. aeruginosa* is one of the most difficult infections to treat due to its various resisting mechanisms against antibacterial agents [72]. Among several available antibiotics, Gent showed good effectiveness against *P. aeruginosa* [73]. Gent activity stems from its irreversible binding to 30 s ribosomal subunits, inhibiting the production of bacteria protein [74]. As a result, we chose *P. aeruginosa* and Gent as a model system to show the effectiveness of our antibacterial surface treatment. Figure 6a shows the result of the antibacterial study. The Gent-grafted PCL/ES10 scaffolds were shown to have significant antibacterial properties against *P. aeruginosa*. Around 80% reduction was observed 1 h after incubation, which increased to 99.94% after 24 h. This result further confirmed the success of surface activation and the grafting of Gent to the scaffolds. Consequently, these composite scaffolds could effectively be implanted without the risk of bacterial infection.

3.7 Cell Cytotoxicity and Proliferation

Cell cytotoxicity assay was performed by live/dead staining at days 10, 14, and 23 after culture on Gent-grafted PCL/ES10 scaffolds. The cell viability is calculated by counting live and dead cells using ImageJ software (Fig. 6b). The results showed 90.9 ± 5.0, 92.8 ± 2.7, and 93.1 ± 6.0% viability at days 10, 14, and 23, respectively. This showed that the 3D printed composite scaffolds were not toxic to cells. Also, Gent grafting did not adversely affect cell survival. Moreover, the confocal microscopy images of the cultured scaffolds showed that fibroblast cells preserved their natural spindle-like shape morphology, showing that the bioactive scaffolds improved cell

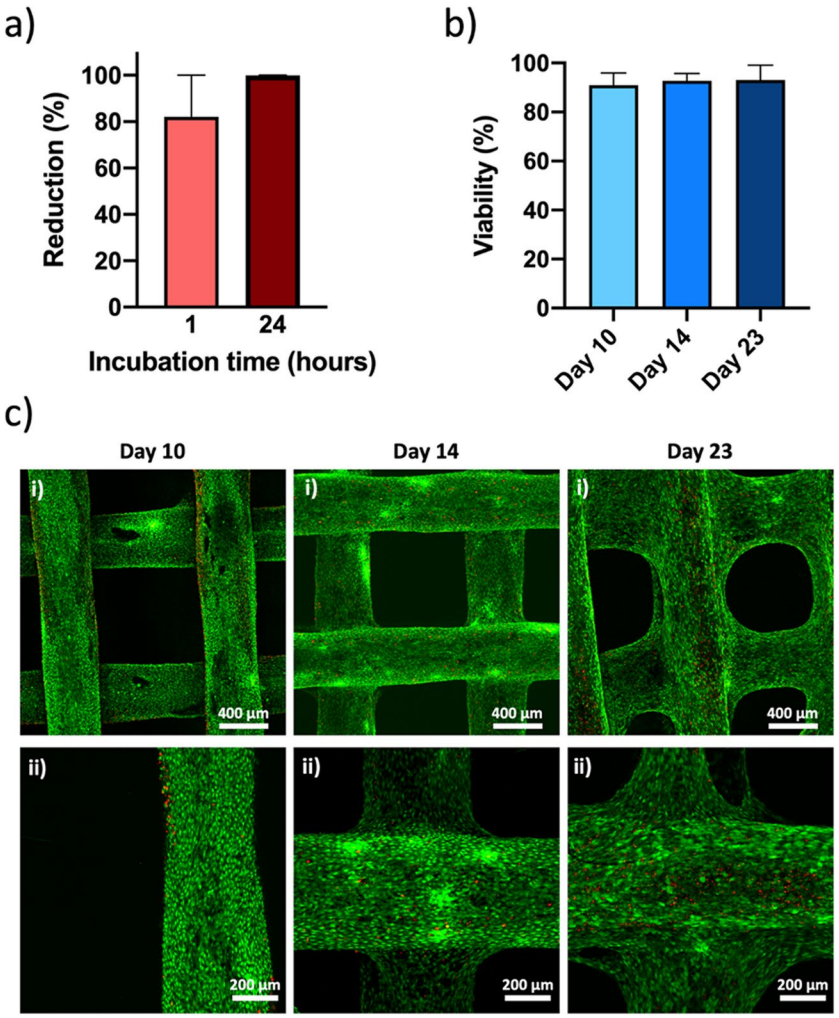

Fig. 6 Assessment of the bioactivity of the plasma treated-PCL/ES10 scaffolds. (**a**) Antibacterial property of Gent-grafted PCL/ES10 scaffolds against P. aeruginosa after 1 and 24 h of incubation. (**b**) Calculated cell viability for fibroblasts cultured on gentamicin grafted PCL/ES10 scaffolds over time and (**c**) representative maximum intensity projection live/dead assay images after 10, 14, and 23 days of cell culture. at (i) low and (ii) high magnifications. Statistical analysis revealed no statistically significant difference between the groups

adhesion and growth. The cells covered the surface of the scaffold by day 10. On day 14, the cells started bridging between filaments to fill the pores, as seen at the corner of the pores (Fig. 6c). On day 23, the bridging was more evident; fibroblasts significantly filled the voids and changed the pore shape from square-like to circular. Further z-stack images in 3D showed that cells kept their phenotype and proliferation potentials (Video S1–4, Supporting Information). These observations could be attributed to changes imposed on the scaffolds through plasma polymerization and Gent grafting. As shown with XPS results, plasma polymerization and Gent grafting introduce different functional groups, such as hydroxyl, carboxyl, and amines, to the surface of the scaffolds. These groups can promote surface properties, affecting hydrophilicity, protein adsorption, and cell-scaffold interaction. Consequently, they could enhance cell binding to the surface of the scaffolds and support prolonged cell viability and proliferation on the substrates [45, 75]. Overall, these results showed that the Gent-grafted PCL/ES10 scaffolds are biocompatible.

3.8 Stem/Stromal Cell Differentiation

Following the cytotoxicity assessment and the confirmation of biocompatibility of the Gent-grafted PCL/ES10 scaffolds with fibroblast cells, the potential of 3D printed scaffolds for bone tissue engineering applications was assessed by culturing hBMSCs on Gent-grafted PCL/ES10 scaffolds and differentiating them toward osteoblasts using ODM.

Figure 7 shows the obtained RT-qPCR data for the expression of osteogenic genes, namely runt-related transcription factor 2 (RUNX2), alkaline phosphatase (ALP), and osteocalcin (OCN), among tested groups. The expression of RUNX2 and OCN was upregulated in groups exposed to ODM for 21 days. In 2D cultures, exposure to ODM resulted in a 5.6-fold increase in OCN and a 7.8-fold increase in RUNX2 expression in hBMSCs + ODM compared to hBMSCs + CM group. On the other hand, in 3D cultures, comparing Gent-grafted PCL/ES10 samples + ODM ($N = 3$) with Gent-grafted PCL/ES10 + CM, a 22.6-fold and 5.3-fold increase in OCN and RUNX2 was observed in the former group. RUNX2 is one of the main transcription

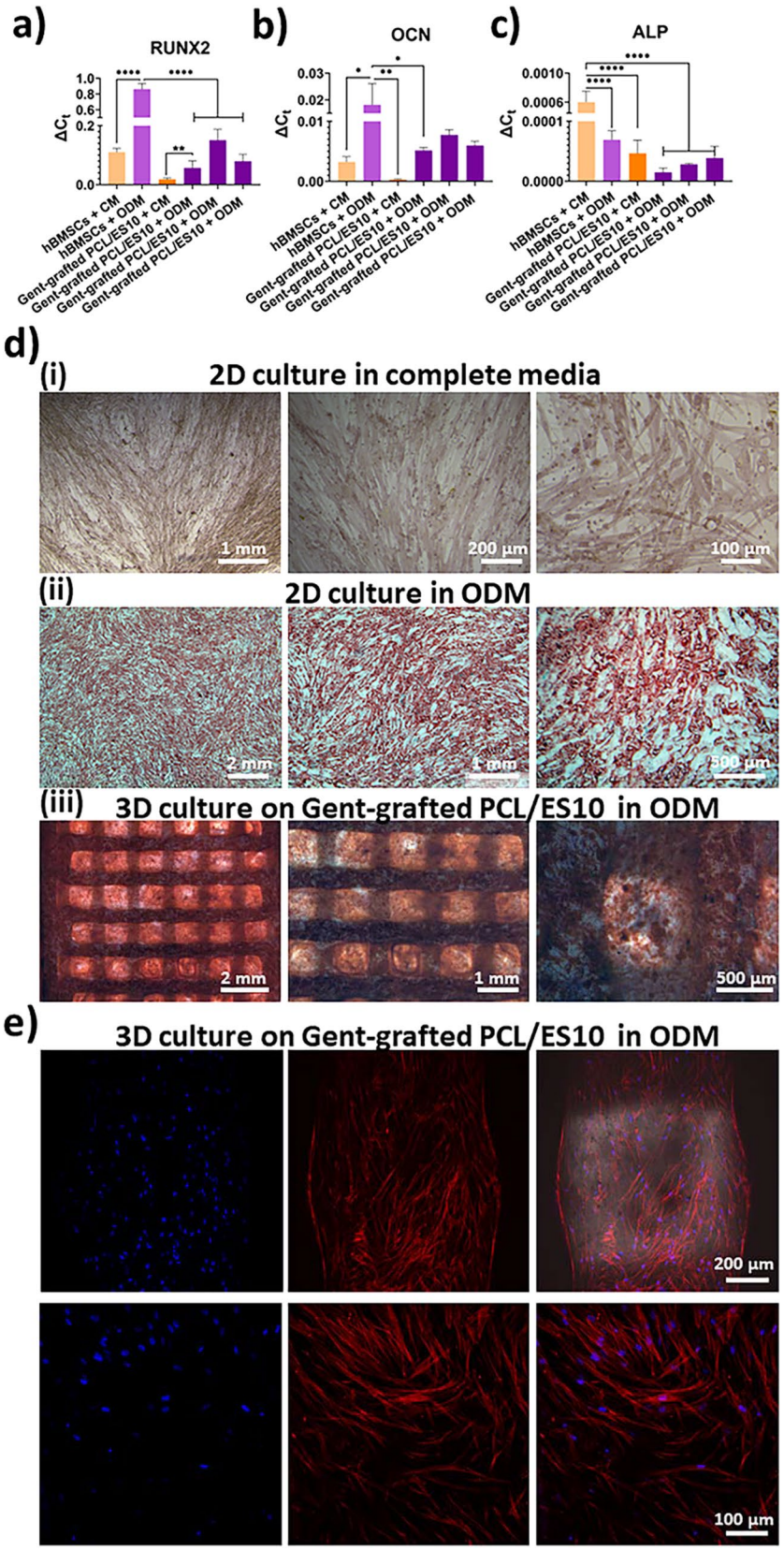

Fig. 7 Osteogenic differentiation of the hBMSCs cultured on the scaffolds. RT-qPCR analysis for gene expression of (**a**) RUNX2, (**b**) OCN, and (**c**) ALP. (**d**) Alizarin red S staining for (i) hBMSCs cultured in 2D in complete media (CM), (ii) hBMSCs cultured in 2D in ODM, and (iii) hBMSCs cultured in 3D in ODM for 21 days. (**e**) Immunofluorescent staining of phalloidin (red) and DAPI (blue) of hBMSCs cultured on Gent-grafted PCL/ES10 after 21 days in ODM

factors influencing and regulating osteogenic differentiation toward osteoblasts, osteoclasts, and osteocytes [76]. Besides, OCN is considered the marker representing a fully differentiated osteoblast [77]. The higher fold change of OCN in 3D culture may signify a higher differentiation efficiency. Interestingly, the ALP expression was significantly lower in all the groups, with the highest expression in 2D culture in growth media (i.e., hBMSCs + CM). ALP is known as an early osteogenic differentiation marker [78]. Previous studies have shown the expression of ALP at the early stages of the differentiation and its downregulation in later time points [79]. Moreover, the upregulation of certain genes like OCN could reduce ALP expression [80]. These results show that exposure to ODM could significantly enhance the osteogenic differentiation of hBMSCs. Besides, a comparison of 2D and 3D cultures showed a reduction in gene expression of all tested genes in 3D cultures. This could be attributed to a change from 2 to 3D culture as well as to the lower stiffness of the scaffolds compared to tissue culture plates. It is well-known that higher stiffness supports osteogenic differentiation [81].

We also investigated the in vitro mineralization using Alizarin Red S staining (Fig. 7). Alizarin Red S staining is used to visualize the deposition of calcium and mineralization of the ECM to represent the later stage of osteogenic differentiation [82]. Secreted mineral crystals are stained red using this technique. hBMSCs cultured in growth media showed no signs of mineral nodule formation, revealing limited signs of osteogenic differentiation. On the other hand, abundant mineralization is observed for both 2D and 3D cultures in ODM. An increase in the intensity of red spots was observed in 3D culture compared to 2D, suggesting upregulated mineralization in 3D. In addition, red spots were present both on the surface of the printed filaments and on the pores covered with cells, which further confirmed the successful differentiation of hBMSCs on Gent-grafted PCL/ES10 scaffolds.

Finally, the adhesion of hBMSCs to the PCL/ES10 scaffolds and cell phenotype was evaluated by visualizing filamentous actin (F-actin) through phalloidin staining. F-actin staining can be leveraged to show the cytoskeleton organization [83]. hMSCs could not only adhere and proliferate on the surface of the printed scaffolds but also bridge the gaps (pores made by mesh printing) and form a confluent layer to fill the pores (Fig. 7). More interestingly, a z-stack using confocal microscopy showed that cells could grow in 3D and fill the gaps at various levels (Video S5, Supporting Information). Moreover, cells showed signs of alignments toward filament orientation at the borders of the filament and pores. This observation suggested that the microstructure of the printed scaffold could influence cell orientation and be leveraged in our future studies to induce anisotropy of ECM depiction inside the printed tissue-engineered scaffold.

4 Conclusions

We reported that 3D printing using ES powder and PCL was a promising technique for creating tissue-engineered scaffolds for bone regeneration. Our results suggested that ES incorporation into PCL can significantly alter the surface topography of the 3D printed scaffolds. Besides, the incorporation of around 30% of ES resulted in agglomerations of the particles during the printing. On the other hand, the mechanical properties were not affected significantly by ES incorporation (10–30 wt.%), and the compressive modulus for the scaffolds was between 16 and 20.1 MPa. The scaffold's bioactivity was significantly improved using plasma polymerization to modify the surface and grafting gentamicin. Upon plasma polymerization, surface hydrophilicity was enhanced drastically, changing the water contact angle from 93.1° to zero. The scaffold also exhibited excellent biocompatibility with cell viability over 90%. Besides, scaffolds supported cell adhesion, proliferation, and osteoblast differentiation, indicating its potential application for bone tissue engineering. Overall, the results suggested that the 3D printed scaffold has shown great potential in the field of bone tissue engineering and could be a significant step toward developing effective treatments for bone regeneration. Further in vivo evaluations are necessary to have a more comprehensive conclusion on the effectiveness of the fabricated scaffolds for bone regeneration. Thus, in continuation of this research, we are planning to perform animal studies using rat models of critically-sized bone defects. The in vivo evaluations can provide us with a more in-depth understanding of the behavior of these composite scaffolds in a physiologically relevant environment.

Supplementary Information The online version contains supplementary material available at https://doi.org/10.1007/s42114-024-00932-4.

Author Contributions Conceptualization: Arman Jafari, Armin Amirsadeghi, Houman Savoji. Methodology: Arman Jafari, Houman Savoji. Formal analysis and investigation: Arman Jafari, Aram-Sevag Afarian, Patrick Piet van Vliet, Mahdi Darvish, Sean Watson. Visualization: Arman Jafari, Houman Savoji. Writing—original draft preparation: Armin Amirsadeghi, Arman Jafari. Writing—review, and editing: Houman Savoji, Vahid Niknezhad, Patrick Piet van Vliet, Gregor Andelfinger, Stephan Reuter, Michael R Wertheimer, Abdellah Ajji. Funding acquisition: Houman Savoji. Resources: Houman Savoji, Vahid Niknezhad, Ali Mousavi, Gregor Andelfinger, Stephan Reuter, Michael R Wertheimer, Abdellah Ajji. Supervision and Resources: Houman Savoji.

Funding This work was financially supported by the Natural Sciences and Engineering Research Council of Canada (NSERC) (NSERC, RGPIN-2021–03960, DGECR-2021–00337), Fonds de Recherche du Québec Santé (FRQS) (Chercheurs-boursiers J1 (313837)), Establishment of Young Investigators (324277), Montreal TransMedTech Institute (iTMT), CRCHU Sainte Justine (CRCHUSJ), and University of Montreal. A.J. gratefully is grateful to the Fonds de Recherche du Québec—Santé (FRQS) Doctoral Scholarship and the Merit Scholarship of the Faculty of Medicine of the University of Montreal.

Data Availability The data supporting this study's findings are available from the corresponding author on reasonable request.

Declarations

Conflict of Interest The authors declare no conflict of interest.

References

1. O'brien FJ (2011) Biomaterials, scaffolds for tissue engineering. Mater Today 14(3):88–95
2. Chen G, Ushida T, Tateishi T (2001) Development of biodegradable porous scaffolds for tissue engineering. Mater Sci Eng C 17(1–2):63–69
3. Gutiérrez-Sánchez M, Escobar-Barrios VA, Pozos-Guillén A, Escobar-García DM (2019) RGD-functionalization of PLA/starch scaffolds obtained by electrospinning and evaluated in vitro for potential bone regeneration. Mater Sci Eng C 96:798–806
4. Ruiz-Alonso S, Lafuente-Merchan M, Ciriza J, Saenz-del-Burgo L, Pedraz JL (2021) Tendon tissue engineering: Cells, growth factors, scaffolds and production techniques. J Control Release 333:448–486
5. Chung HJ, Park TG (2007) Surface engineered and drug releasing pre-fabricated scaffolds for tissue engineering. Adv Drug Del Rev 59(4–5):249–262
6. Qu H (2020) Additive manufacturing for bone tissue engineering scaffolds. Mater Today Commun 24:101024
7. Manavitehrani I, Le TY, Daly S, Wang Y, Maitz PK, Schindeler A, Dehghani F (2019) Formation of porous biodegradable scaffolds based on poly (propylene carbonate) using gas foaming technology. Mater Sci Eng C 96:824–830
8. Zhang Z, Feng Y, Wang L, Liu D, Qin C, Shi Y (2022) A review of preparation methods of porous skin tissue engineering scaffolds. Mater Today Commun 32:104109
9. Liang H, Mirinejad MS, Asefnejad A, Baharifar H, Li X, Saber-Samandari S, Toghraie D, Khandan A (2022) Fabrication of tragacanthin gum-carboxymethyl chitosan bio-nanocomposite wound dressing with silver-titanium nanoparticles using freeze-drying method. Mater Chem Phys 279:125770
10. Zieliński PS, Gudeti PKR, Rikmanspoel T, Włodarczyk-Biegun MK (2023) 3D printing of bio-instructive materials: Toward directing the cell. Bioact Mater 19:292–327
11. Jafari A, Ajji Z, Mousavi A, Naghieh S, Bencherif SA, Savoji H (2022) Latest Advances in 3D Bioprinting of Cardiac Tissues. Adv Mater Technol 7(11):2101636
12. Jafari A, Farahani M, Sedighi M, Rabiee N, Savoji H (2022) Carrageenans for tissue engineering and regenerative medicine applications: A review. Carbohydr Polym 281:119045
13. Khan MUA, Haider S, Haider A, Abd Razak SI, Kadir MRA, Shah SA, Javed A, Shakir I, Al-Zahrani AA (2021) Development of porous, antibacterial and biocompatible GO/n-HAp/bacterial cellulose/β-glucan biocomposite scaffold for bone tissue engineering. Arabian Journal of Chemistry 14(2):102924
14. Yousefiasl S, Sharifi E, Salahinejad E, Makvandi P, Irani S (2023) Bioactive 3D-printed chitosan-based scaffolds for personalized craniofacial bone tissue engineering. Eng Regen 4(1):1–11
15. Aslam Khan MU, Mehboob H, Abd Razak SI, Yahya MY, Mohd Yusof AH, Ramlee MH, Sahaya Anand TJ, Hassan R, Aziz A, Amin R (2020) Development of polymeric nanocomposite (xyloglucan-co-methacrylic acid/hydroxyapatite/sio2) scaffold for bone tissue engineering applications—in-vitro antibacterial, cytotoxicity and cell culture evaluation. Polymers 12(6):1238
16. Khan MUA, Haider S, Shah SA, Abd Razak SI, Hassan SA, Kadir MRA, Haider A (2020) Arabinoxylan-co-AA/HAp/TiO2 nanocomposite scaffold a potential material for bone tissue engineering: An in vitro study. Int J Biol Macromol 151:584–594
17. Salhotra A, Shah HN, Levi B, Longaker MT (2020) Mechanisms of bone development and repair. Nat Rev Mol Cell Biol 21(11):696–711
18. Aslam Khan MU, Al-Arjan WS, Binkadem MS, Mehboob H, Haider A, Raza MA, Abd Razak SI, Hasan A, Amin R (2021) Development of biopolymeric hybrid scaffold-based on AAc/GO/nHAp/TiO2 nanocomposite for bone tissue engineering: In-vitro analysis. Nanomaterials 11(5):1319
19. Khan MU, Abd Razak SI, Mehboob H, Abdul Kadir MR, Anand TJ, Inam F, Shah SA, Abdel-Haliem ME, Amin R (2021) Synthesis and characterization of silver-coated polymeric scaffolds for bone tissue engineering: antibacterial and in vitro evaluation of cytotoxicity and biocompatibility. ACS omega 6(6):4335–4346
20. Khan MUA, Raza MA, Mehboob H, Kadir MRA, Abd Razak SI, Shah SA, Iqbal MZ, Amin R (2020) Development and in vitro evaluation of κ-carrageenan based polymeric hybrid nanocomposite scaffolds for bone tissue engineering. RSC Adv 10(66):40529–40542
21. Khan MUA, Abd Razak SI, Rehman S, Hasan A, Qureshi S, Stojanović GM (2022) Bioactive scaffold (sodium alginate)-g-(nHAp@ SiO2@ GO) for bone tissue engineering. Int J Biol Macromol 222:462–472
22. Khan MUA, Rizwan M, Razak SIA, Hassan A, Rasheed T, Bilal M (2022) Electroactive polymeric nanocomposite BC-g-(Fe3O4/GO) materials for bone tissue engineering: in vitro evaluations. J Biomater Sci Polym Ed 33(11):1349–1368
23. Javid-Naderi MJ, Behravan J, Karimi-Hajishohreh N, Toosi S (2023) Synthetic polymers as bone engineering scaffold. Polym Adv Technol 34(7):2083–2096
24. Gatto ML, Furlani M, Giuliani A, Bloise N, Fassina L, Visai L, Mengucci P (2021) Biomechanical performances of PCL/HA micro-and macro-porous lattice scaffolds fabricated via laser powder bed fusion for bone tissue engineering. Mater Sci Eng C 128:112300
25. Cestari F, Petretta M, Yang Y, Motta A, Grigolo B, Sglavo VM (2021) 3D printing of PCL/nano-hydroxyapatite scaffolds derived from biogenic sources for bone tissue engineering. Sustain Mater Technol 29:e00318
26. Yang X, Wang Y, Zhou Y, Chen J, Wan Q (2021) The application of polycaprolactone in three-dimensional printing scaffolds for bone tissue engineering. Polymers 13(16):2754
27. Murugan S, Parcha SR (2021) Fabrication techniques involved in developing the composite scaffolds PCL/HA nanoparticles for bone tissue engineering applications. J Mater Sci Mater Med 32(8):93
28. Cree D, Rutter A (2015) Sustainable bio-inspired limestone eggshell powder for potential industrialized applications. ACS Sustain Chem Eng 3(5):941–949
29. Hossain MS, Shaikh MAA, Ahmed S (2023) Synthesis of gypsum fertilizer from waste eggshells for a sustainable environment. Mater Adv 4(1):240–247
30. Wu S-C, Tsou H-K, Hsu H-C, Hsu S-K, Liou S-P, Ho W-F (2013) A hydrothermal synthesis of eggshell and fruit waste extract to produce nanosized hydroxyapatite. Ceram Int 39(7):8183–8188
31. Huang Y-Z, Ji Y-R, Kang Z-W, Li F, Ge S-F, Yang D-P, Ruan J, Fan X-Q (2020) Integrating eggshell-derived CaCO3/MgO nanocomposites and chitosan into a biomimetic scaffold for bone regeneration. Chem Eng J 395:125098
32. Wu X, Stroll SI, Lantigua D, Suvarnapathaki S, Camci-Unal G (2019) Eggshell particle-reinforced hydrogels for bone tissue engineering: An orthogonal approach. Biomater Sci 7(7):2675–2685

33. Zhou W, Peng X, Ma Y, Hu Y, Wu Y, Lan F, Weir MD, Li M, Ren B, Oates TW (2020) Two-staged time-dependent materials for the prevention of implant-related infections. Acta Biomater 101:128–140
34. Seebach E, Kubatzky KF (2019) Chronic implant-related bone infections—can immune modulation be a therapeutic strategy? Front Immunol 10:1724
35. Khan MUA, Al-Arjan WS, Ashammakhi N, Haider S, Amin R, Hasan A (2022) Multifunctional bioactive scaffolds from ARX-g-(Zn@ rGO)-HAp for bone tissue engineering: In vitro antibacterial, antitumor, and biocompatibility evaluations. ACS Appl Bio Mater 5(11):5445–5456
36. Paris JL, Lafuente-Gómez N, Cabañas MV, Román J, Peña J, Vallet-Regí M (2019) Fabrication of a nanoparticle-containing 3D porous bone scaffold with proangiogenic and antibacterial properties. Acta Biomater 86:441–449
37. López-Pérez PM, Da Silva RM, Sousa RA, Pashkuleva I, Reis RL (2010) Plasma-induced polymerization as a tool for surface functionalization of polymer scaffolds for bone tissue engineering: an in vitro study. Acta Biomater 6(9):3704–3712
38. Asadian M, Chan KV, Norouzi M, Grande S, Cools P, Morent R, De Geyter N (2020) Fabrication and plasma modification of nanofibrous tissue engineering scaffolds. Nanomaterials 10(1):119
39. Truica-Marasescu F, Girard-Lauriault P-L, Lippitz A, Unger WE, Wertheimer MR (2008) Nitrogen-rich plasma polymers: Comparison of films deposited in atmospheric-and low-pressure plasmas. Thin Solid Films 516(21):7406–7417
40. Truica-Marasescu F, Wertheimer MR (2008) Nitrogen-rich plasma-polymer films for biomedical applications. Plasma Processes Polym 5(1):44–57
41. Ruiz JC, St-Georges-Robillard A, Thérésy C, Lerouge S, Wertheimer MR (2010) Fabrication and characterisation of amine-rich organic thin films: Focus on stability. Plasma Processes Polym 7(9–10):737–753
42. Ruiz JC, Girard-Lauriault PL, Wertheimer MR (2015) Fabrication, characterization, and comparison of oxygen-rich organic films deposited by plasma-and vacuum-ultraviolet (VUV) photopolymerization. Plasma Processes Polym 12(3):225–236
43. Lerouge S, Barrette J, Ruiz JC, Sbai M, Savoji H, Saoudi B, Gauthier M, Wertheimer MR (2015) Nitrogen-Rich Plasma Polymer Coatings for Biomedical Applications: Stability, Mechanical Properties and Adhesion Under Dry and Wet Conditions. Plasma Processes Polym 12(9):882–895
44. Siow KS, Britcher L, Kumar S, Griesser HJ (2006) Plasma methods for the generation of chemically reactive surfaces for biomolecule immobilization and cell colonization-a review. Plasma Processes Polym 3(6–7):392–418
45. Savoji H, Hadjizadeh A, Maire M, Ajji A, Wertheimer MR, Lerouge S (2014) Electrospun nanofiber scaffolds and plasma polymerization: a promising combination towards complete, stable endothelial lining for vascular grafts. Macromol Biosci 14(8):1084–1095
46. Savoji H, Maire M, Lequoy P, Liberelle B, De Crescenzo G, Ajji A, Wertheimer MR, Lerouge S (2017) Combining electrospun fiber mats and bioactive coatings for vascular graft prostheses. Biomacromol 18(1):303–310
47. Scaffaro R, Lopresti F, Sutera A, Botta L, Fontana RM, Gallo G (2017) Plasma modified PLA electrospun membranes for actinorhodin production intensification in Streptomyces coelicolor immobilized-cell cultivations. Colloids Surf B Biointerfaces 157:233–241
48. Ghorbani F, Sahranavard M, Zamanian A (2020) Immobilization of gelatin on the oxygen plasma-modified surface of polycaprolactone scaffolds with tunable pore structure for skin tissue engineering. J Polym Res 27:1–12
49. Murab S, Gruber SM, Lin C-YJ, Whitlock P (2020) Elucidation of bio-inspired hydroxyapatie crystallization on oxygen-plasma modified 3D printed poly-caprolactone scaffolds. Mater Sci Eng C 109:110529
50. Khoshroo K, Kashi TSJ, Moztarzadeh F, Tahriri M, Jazayeri HE, Tayebi L (2017) Development of 3D PCL microsphere/TiO2 nanotube composite scaffolds for bone tissue engineering. Mater Sci Eng C 70:586–598
51. Permyakova ES, Kiryukhantsev-Korneev PV, Ponomarev VA, Sheveyko AN, Dobrynin SA, Polčak J, Slukin PV, Ignatov SG, Manakhov A, Kulinich SA (2021) Antibacterial activity of therapeutic agent-immobilized nanostructured TiCaPCON films against antibiotic-sensitive and antibiotic-resistant Escherichia coli strains. Surf Coat Technol 405:126538
52. Jafari A, Amirsadeghi A, Hassanajili S, Azarpira N (2020) Bioactive antibacterial bilayer PCL/gelatin nanofibrous scaffold promotes full-thickness wound healing. Int J Pharm 583:119413
53. Abasalta M, Asefnejad A, Khorasani MT, Saadatabadi AR, Irani M (2022) Adsorption and sustained release of doxorubicin from N-carboxymethyl chitosan/polyvinyl alcohol/poly (ε-caprolactone) composite and core-shell nanofibers. J Drug Deliv Sci Technol 67:102937
54. Habte L, Shiferaw N, Mulatu D, Thenepalli T, Chilakala R, Ahn JW (2019) Synthesis of nano-calcium oxide from waste eggshell by sol-gel method. Sustainability 11(11):3196
55. Kumar V, Dev A, Gupta A (2014) Studies of poly (lactic acid) based calcium carbonate nanocomposites. Compos B Eng 56:184–188
56. Kim HS, Park BH, Choi JH, Yoon JS (2008) Mechanical properties and thermal stability of poly (L-lactide)/calcium carbonate composites. J Appl Polym Sci 109(5):3087–3092
57. Dávila JL, Freitas MS, Inforçatti Neto P, Silveira ZC, Silva JVL, d'Ávila MA (2016) Fabrication of PCL/β-TCP scaffolds by 3D mini-screw extrusion printing. J Appl Polym Sci 133:43031
58. Zhang Y, Li H, Zhang Y, Song F, Cao X, Lyu X, Zhang Y, Crittenden J (2018) Statistical optimization and batch studies on adsorption of phosphate using Al-eggshell. Adsorpt Sci Technol 36(3–4):999–1017
59. Balu R, Kumar T, Ramalingam M, Ramakrishna S (2011) Electrospun Polycaprolactone/Poly (1, 4-butylene adipate-co-polycaprolactam) blends: Potential biodegradable scaffold for bone tissue regeneration. J Biomater Tissue Eng 1(1):30–39
60. Arraiza AL, Sarasua J, Verdu J, Colin X (2007) Rheological behavior and modeling of thermal degradation of poly (ϵ-caprolactone) and poly (L-lactide). Int Polym Proc 22(5):389–394
61. Wong A-Y (1998) Factors affecting extrudate swell and melt flow rate. J Mater Process Technol 79(1–3):163–169
62. Kim JH, Ahn JH, Hong JS, Ahn KH (2020) Change of rheological/mechanical properties of poly (caprolactone)/CaCO 3 composite with particle surface modification. Korea-Australia Rheology Journal 32:29–39
63. Liang J-Z, Zhou L, Tang C-Y, Tsui C-P, Li F-J (2012) Melt flow behavior in capillary extrusion of nanometer calcium carbonate filled PCL bio-composites. Polym Test 31(1):149–154
64. Qiao R, Deng H, Putz KW, Brinson LC (2011) Effect of particle agglomeration and interphase on the glass transition temperature of polymer nanocomposites. J Polym Sci Part B: Polym Phys 49(10):740–748
65. Karbowniczek JE, Ura DP, Stachewicz U (2022) Nanoparticles distribution and agglomeration analysis in electrospun fiber based composites for desired mechanical performance of poly (3-hydroxybuty-rate-co-3-hydroxyvalerate (PHBV) scaffolds with hydroxyapatite (HA) and titanium dioxide (TiO2) towards medical applications. Compos B Eng 241:110011

66. Murizan NIS, Mustafa NS, Ngadiman NHA, Mohd Yusof N, Idris A (2020) Review on nanocrystalline cellulose in bone tissue engineering applications. Polymers 12(12):2818
67. Yang W-Q, Zeng N-X, Mei H, Chen C, Lin X, Cheng L-F (2019) Designable mechanical properties of 3D printing composites with multiple filaments by different infill percentages and structures. Adv Eng Mater 21(10):1900508
68. Algarni M, Ghazali S (2021) Comparative study of the sensitivity of PLA, ABS, PEEK, and PETG's mechanical properties to FDM printing process parameters. Crystals 11(8):995
69. Boespflug G, Maire M, De Crescenzo G, Lerouge S, Wertheimer MR (2017) Characterization and comparison of N-, O-, and N+ O-functionalized polymer surfaces for efficient (HUVEC) endothelial cell colonization. Plasma Processes Polym 14(7):1600139
70. Permyakova ES, Manakhov AM, Kiryukhantsev-Korneev PV, Sheveyko AN, Gudz KY, Kovalskii AM, Polčak J, Zhitnyak IY, Gloushankova NA, Dyatlov IA (2021) Different concepts for creating antibacterial yet biocompatible surfaces: Adding bactericidal element, grafting therapeutic agent through COOH plasma polymer and their combination. Appl Surf Sci 556:149751
71. Triffault-Fillit C, Ferry T, Laurent F, Pradat P, Dupieux C, Conrad A, Becker A, Lustig S, Fessy M-H, Chidiac C (2019) Microbiologic epidemiology depending on time to occurrence of prosthetic joint infection: a prospective cohort study. Clin Microbiol Infect 25(3):353–358
72. Cerioli M, Batailler C, Conrad A, Roux S, Perpoint T, Becker A, Triffault-Fillit C, Lustig S, Fessy M-H, Laurent F (2020) Pseudomonas aeruginosa implant-associated bone and joint infections: Experience in a regional reference center in France. Front Med 7:513242
73. Sudduth JD, Moss JA, Spitler CA, Pham V-LH, Jones LC, Brown JT, Bergin PF (2020) Open fractures: are we still treating the same types of infections? Surg Infect (Larchmt) 21(9):766–772
74. Buechler CR, Daveluy SD (2022) 15 - topical therapeutics. In: Shi VY, Hsiao JL, Lowes MA, Hamzavi IH (eds) A comprehensive guide to hidradenitis suppurativa. Elsevier, Philadelphia, pp 145–154.
75. Antonini V, Torrengo S, Marocchi L, Minati L, Dalla Serra M, Bao G, Speranza G (2014) Combinatorial plasma polymerization approach to produce thin films for testing cell proliferation. Colloids Surf. B. Biointerfaces 113:320–329
76. Narayanan A, Srinaath N, Rohini M, Selvamurugan N (2019) Regulation of Runx2 by MicroRNAs in osteoblast differentiation. Life Sci 232:116676
77. Aghajanpour S, Esfandyari-Manesh M, Ghahri T, Ghahremani MH, Atyabi F, Heydari M, Motasadizadeh H, Dinarvand R (2022) Impact of oxygen-calcium-generating and bone morphogenetic protein-2 nanoparticles on survival and differentiation of bone marrow-derived mesenchymal stem cells in the 3D bio-printed scaffold. Colloids Surf B Biointerfaces 216:112581
78. Meesuk L, Suwanprateeb J, Thammarakcharoen F, Tantrawatpan C, Kheolamai P, Palang I, Tantikanlayaporn D, Manochantr S (2022) Osteogenic differentiation and proliferation potentials of human bone marrow and umbilical cord-derived mesenchymal stem cells on the 3D-printed hydroxyapatite scaffolds. Sci Rep 12(1):19509
79. Chen M, Le DQ, Kjems J, Bünger C, Lysdahl H (2015) Improvement of distribution and osteogenic differentiation of human mesenchymal stem cells by hyaluronic acid and β-tricalcium phosphate-coated polymeric scaffold in vitro. BioResearch Open Access 4(1):363–373
80. Vimalraj S (2020) Alkaline phosphatase: Structure, expression and its function in bone mineralization. Gene 754:144855
81. Ferlin KM, Prendergast ME, Miller ML, Kaplan DS, Fisher JP (2016) Influence of 3D printed porous architecture on mesenchymal stem cell enrichment and differentiation. Acta Biomater 32:161–169
82. Xu Z, Lin B, Zhao C, Lu Y, Huang T, Chen Y, Li J, Wu R, Liu W, Lin J (2022) Lanthanum doped octacalcium phosphate/polylactic acid scaffold fabricated by 3D printing for bone tissue engineering. J Mater Sci Technol 118:229–242
83. Huang Z, He Y, Chang X, Liu J, Yu L, Wu Y, Li Y, Tian J, Kang L, Wu D (2020) A magnetic iron oxide/polydopamine coating can improve osteogenesis of 3D-printed porous titanium scaffolds with a static magnetic field by upregulating the TGFβ-smads pathway. Adv Healthc Mater 9(14):2000318